YTUP

Journal of Thermal Engineering
https://jten.yildiz.edu.tr/
https://doi.org/10.47481/jten.0050

RESEARCH ARTICLE

The use of thermal mass effect to reduce heating demand in charcoal cookstoves

Lomena Mulenda A.[1,2,*], Mbuyi Katshiatshia H.[3], Ndaye Nkanka B.[4], Amsini Sadiki[5,6], Sumuna Temo V.[7]

[1]Centre de Recherche en Energies Renouvelables, Faculté Polytechnique, Université de Kinshasa, Avenue de l'Université N° 01, Commune de Lemba, BP 127 Kinshasa 11, Democratic Republic of the Congo
[2]Centre d'Etudes et de Recherches sur les Energies Renouvelables Kitsisa-Khonde (CERERK), ISTA-Kinshasa, Avenue Aérodrome N° 3930, Commune de Barumbu, BP 6593 Kinshasa 31, Democratic Republic of the Congo
[3]Centre d'Etudes et de Recherches sur les Energies Renouvelables Kitsisa-Khonde (CERERK), ISTA-Kinshasa, Avenue Aérodrome N° 3930, Commune de Barumbu, BP 6593 Kinshasa 31, Democratic Republic of the Congo
[4]Centre d'Etudes et de Recherches sur les Energies Renouvelables Kitsisa-Khonde (CERERK), ISTA-Kinshasa, Avenue Aérodrome N° 3930, Commune de Barumbu, BP 6593 Kinshasa 31, Democratic Republic of the Congo
[5]Institute for Energy and Power Plant Technology, Technische Universität Darmstadt, 64287 Darmstadt, Germany
[6]Institute of Reactive Flows and Diagnostics, Technical University of Darmstadt, 64287 Darmstadt, Germany
[7]Centre de Recherche en Energies Renouvelables, Faculté Polytechnique, Université de Kinshasa, Avenue de l'Université N° 01, Commune de Lemba, BP 127 Kinshasa 11, Democratic Republic of the Congo

Abstract

Thermal mass, defined as the capacity of materials to absorb, store, and radiate heat, plays a critical role in improving the efficiency of biomass cookstoves. This study evaluates the integration of clay liners into charcoal cookstove designs using three methods: analytical modeling, OpenFOAM simulations, and electrical-analogy modeling. Radiation modeling between clay-lined combustion chamber surfaces and the cooking pot was validated experimentally by testing four Jiko-type cookstoves — which featured combustion chambers of different shapes but identical top inner diameters — against a traditional metal stove. ISO Water Heating Tests and Controlled Cooking Tests (CCT) were conducted. Results revealed that the net radiative heat transfer to the pot remained consistent (153 W ± 0.5%), very slightly affected by combustion chamber shape. However, chamber volume and fuel burn duration significantly influenced performance. Clay-lined stoves exhibited 32–59% higher ISO thermal efficiency than metal stoves and achieved 34–47% fuel savings during standard cooking tasks. Notably, inverted-truncated-cone designs achieved 20% greater thermal efficiency than right-circular-cylinder configurations; this improvement is attributable to their reduced volumetric capacity and their resulting fuel economy during CCT. Additionally, the clay lining's radiative effect intensifies over time, resulting in an increase in thermal efficiency of up to 30% during the transition from cold-start to hot-start operational phases.

Keywords: Charcoal cookstoves, clay, thermal mass, transient heat conduction, radiation heat transfer

Cite this article as: Lomena Mulenda, A., Mbuyi Katshiatshia, H., Ndaye Nkanka, B., Amsini, S., & Sumuna Temo, V. (2026). The use of thermal mass effect to reduce heating demand in charcoal cookstoves. Journal of Thermal Engineering, 12(4), 1573–1587. https://doi.org/10.47481/jten.0050

1. Introduction

Biomass remains a vital source of energy for heating and cooking in many countries, with global consumption reaching 34 exajoules (EJ) in 2023 [1–3]. Notably, 17% of all fuelwoods harvested in the world are converted into charcoal, producing an estimated 54.7 million tons annually—of which 64% is consumed in Africa alone [4]. However, the reliance on inefficient, low-quality stoves for charcoal combustion has three severe consequences: (1) environmental degradation as overharvesting of wood for charcoal production accelerates deforestation and climate change [3–5], (2) health hazards with incomplete combustion releasing harmful pollutants as carbon monoxide (CO) and particulate matters ($PM_{2.5}$), linked to respiratory

*Corresponding Author
E-mail Adress: lomena.mulenda@ista.ac.cd

Submitted: 20 February 2025; **Accepted:** 19 August 2025

This paper was recommended for publication in revised form by Editor-in-Chief Ahmet Selim Dalkılıç

diseases [1,6,7], and (3) economic burdens, where fuel expenses can consume up to 40% of household income [8–10]. Addressing these issues requires transformative solutions, and one promising approach leverages an age-old principle: thermal mass [11]. By integrating materials that absorb, store, and gradually release heat, charcoal cookstoves can transform into sustainable powerhouses, reducing emissions, lowering costs and improving livelihoods, particularly for women [1,3].

In cookstoves, thermal mass materials (e.g., clay and ceramics) act as "heat batteries", stabilizing temperatures and extending cooking cycles. A clay-lined stove retains heat long after the charcoal burns out, enabling simmering without additional fuel [5,12]. Studies, such as those on Kenya's ceramic Jiko stoves [8,13], demonstrate 30-50% reductions in charcoal use while also reducing emissions. This effect is likewise present in rocket stoves with heat banks that are used as space heating alternatives in sustainable home design, natural building, or off-grid living [14,15]. Other real-world applications refer to hybrid designs prototypes that integrate thermal mass with solar energy for heat storage during non-sunny periods [11].

Existing literature on biomass cookstoves [16–18] underscores the importance of material selection in stoves performance. Clay, a widely available and sustainable material [10], is recognized for enhancing combustion chamber efficiency. Studies by Still et al. [18,19] showed that ceramic mixes made from clay insulation and common ceramic bricks for rocket wood-burning stoves combustion chambers achieve higher exit gas temperatures. Similarly, Odesola et al. [12] in 2019 and Boafo-Mensah et al. [5]in 2020, reported that ceramic clay linings improve combustion chamber performance. However, the integration of clay as thermal mass in stove design encounters significant challenges, primarily due to its high density, which contributes to increased stove weight and elevated production costs [20]. Drawing on a synthesis of prior research, Irro et al. [21] emphasized that stoves built from heavyweight materials may be more fuel consuming, as a portion of useful heat is absorbed by the material itself, reducing fuel efficiency. Recent works have explored lightweight alternatives. For instance, Okino et al. in 2021 [22] and Kyuvi et al. in 2023 [20] demonstrated that incorporating carbonized organic waste additives (e.g., sawdust, char) into clay matrices can improve insulation properties by reducing bulk density and increasing porosity during the firing process. Additionally, lightweight insulation materials, such as perlite, vermiculite, and ceramic wool, have also shown promise in enabling high-efficiency, low-mass stove designs [23]. Nevertheless, scalability barriers persist in low-income regions, where reliance on these imported materials imposes prohibitive costs, thereby limiting their economic viability and geographic accessibility [13]. By contrast, clay-lined stoves remain a culturally adapted, low-tech and low-cost solution, solidifying their role as a cornerstone of clean cooking interventions [5].

To be effective, thermal mass must be combined with other passive design principles – such as optimized geometry and surface orientation [5,11,21,23]. Despite progress in thermal science and cookstove engineering, critical knowledge gaps persist in understanding thermal-mass mechanisms, particularly (i) modeling heat storage and radiative exchange between clay-lined combustion-chamber surfaces and the cooking pot, and (ii) analyzing how stove combustion-chamber geometry (shape, volume) and pot configuration affect performance. This study addresses these gaps through a dual approach: (1) Modeling—analytical, numerical (OpenFOAM-based CFD), and electrical analogy methods are employed to analyze transient heat conduction, radiative transfer, and system dynamics. In this work, the electrical-analogy model provides a state-space description of the cookstove's thermal system, with heat-storage elements as state variables, while a radiative model quantifies heat exchange between passive surfaces. (2) Experimentation: Four cookstove prototypes are evaluated against the traditional metal model using ISO 19867-1 Water Heating Tests (thermal efficiency) [24] and Controlled Cooking Tests (fuel savings) [25], with a focus on inverted-truncated-cone versus cylindrical combustion chambers.

This work aims to advance scalable, low-cost, and high efficiency cookstoves by elucidating heat storage dynamics and radiative transfer mechanisms. The paper is structured as follows: Section 2 details the materials and methods; Section 3 presents the results and discussions. Section 4 outlines limitations of this work, and Section 5 is devoted to conclusions.

2. Material and Method

2.1. Transient heat conduction modeling

2.1. 1. A 1-D simplified analytical model in thermal mass

Thermal mass modulates thermal energy storage by absorbing and releasing heat in response to temperature fluctuations. This section examines how placing thermal mass near the fire affects its thermal response. The transient conduction behavior of the thermal mass can be modeled as one-dimensional heat conduction through a slab, assuming no internal heat generation and time-dependent temperature variation at one boundary [26–30].

The transient heat diffusion equation is:

$$\frac{\partial T}{\partial t} = \alpha \frac{\partial^2 T}{\partial x^2} \tag{1}$$

where α is the thermal diffusivity of the material ($m^2 \cdot s^{-1}$) such as $\alpha = k/\rho c$, and k is its thermal conductivity ($W \cdot m^{-1} \cdot K^{-1}$), ρ its density ($kg \cdot m^{-3}$), c its specific thermal capacity ($J \cdot kg^{-1} \cdot K^{-1}$).

The system is governed by the following conditions:

$$T(0,t) = \begin{cases} B & \text{for } t = 0 \text{ (steady - state in the slab)} \\ \varphi(t) & \text{for } 0 < t < \infty \end{cases} \tag{2}$$

$$-k\frac{\partial T}{x}(L,t) = h[T(L,t) - T_\infty] \tag{3}$$

$$T(x,0) = f(x), \text{ for } 0 < x \leq L \quad (4)$$

Prior to t = 0, the inner surface of the slab (x = 0) was maintained at a constant temperature, B , determined by a surface energy balance [27], while the back-side surface (x=L) was subjected to convective heat transfer. The heating duration was sufficient to establish a steady-state temperature distribution within the slab. Then, for t > 0 , the temperature at x=0 begins to decrease as a function of time, φ(t), while the boundary at x=L remains under convective conditions. The heat transfer coefficient is denoted by h ($W \cdot m^{-2} \cdot K^{-1}$) and the ambient temperature T_∞ (K).

For time-dependent boundary conditions, the solution can be derived using Duhamel's theorem [28]. However, if the conduction problem involves a non-zero initial temperature distribution, the superposition principle may be employed to obtain the solution [31,32]. The complete analytical solution to this problem (Equation (5)) is presented in Appendix A.

$$T(x,t) = (T(0,t) - T_\infty) \cdot \left(1 - \frac{Bi}{(1+Bi)}\frac{x}{L}\right) + T_\infty + \sum_{n=1}^{\infty} \frac{2T(0,t)_{,t} L^2}{\alpha(\mu_n L)^3}\left[1 - \cos\mu_n L + \frac{Bi(\mu_n L \cos\mu_n L - \sin\mu_n L)}{(1+Bi)\mu_n L}\right]\left(e^{-\alpha\mu_n^2 t} - 1\right)\sin\mu_n x \quad (5)$$

Here the $\mu_n L$ are the typical roots to the transcendental equation:

$$\tan\mu L = -\frac{1}{Bi}\mu L \quad (6)$$

with Bi the Biot number, by definition $Bi = \frac{hL}{k}$, and μ_n the eigenvalues of the problem. The term $T(0,t)_{,t}$ represents the derivative of $T(0,t)$ in respect with time.

The Robin boundary condition (or convection-type boundary condition) is a general case that encompasses the Neumann condition, which corresponds to specifying the heat flux at the back surface $\frac{\partial T}{\partial n}(L,t)$ as zero (an insulated boundary). This special case is obtained by setting h = 0, which results in Bi = 0. Under these conditions, the roots of the transcendental Equation (6) simplify to $\mu_n L \approx \frac{n\pi}{2}$ [27].

Table 1 presents the solutions for the transient temperature distribution in the slab when a linearly decreasing temperature is imposed over time at the boundary surface x = 0.

$$T(0,t) = \begin{cases} B & \text{for } t = 0 \text{ (steady - state was attained)} \\ At + B & \text{for } 0 < t < \frac{|B - T_\infty|}{A}, \text{ A negative} \end{cases} \quad (7)$$

Table 1. Temperature distribution within a slab under the condition of a linearly time-dependent temperature decrease imposed at one boundary surface.

Initial condition: steady state in the slab, $T(0, t) = At + B$ **(at x = 0)** **Type of boundary condition at x = L**	**Temperature distribution**
Convection (Robin b.c.'s)	$T(x,t) = (At + B - T_\infty) \cdot \left(1 - \frac{-Bi}{(1+Bi)}\frac{-x}{L}\right) + -T_\infty + \sum_{n=1}^{\infty} \frac{2AL^2}{\alpha(\mu_n L)^3}\left[1 - \cos\mu_n L + \frac{Bi(\mu_n L \cos\mu_n L - \sin\mu_n L)}{(1+Bi)\mu_n L}\right]\left(e^{-\alpha\mu_n^2 t} - 1\right)\sin\mu_n x$
Zero heat flux / end insulated (Neumann b.c.'s)	$T(x,t) = (At + B) + \frac{16AL^2}{\alpha\pi^3}\sum_{n=1}^{\infty}\left(\frac{e^{-\alpha\left(\frac{n\pi}{2L}\right)^2 t} - 1}{n^3}\right)\sin\left(\frac{n\pi x}{2L}\right)$

2.1.2. Heat transfer OpenFOAM-based numerical simulations

OpenFOAM is a free, open-source computational fluid dynamics (CFD) software based on finite volume method and implemented in C++ [33,34]. Among its applications, the LaplacianFoam solver is specifically designed to simulate diffusion-driven scalar transport phenomena in both transient and steady-state forms. Unlike many commercial CFD packages, OpenFOAM employs a case-based file-structure rather than a single case file [35]. The geometry can be generated by defining the mesh in the file system's blockMeshDict. The 0 directory contains the initial and boundary conditions for the simulation. The constant directory, in turn, contains files related to the physics of the problem. To implement convective boundary conditions in laplacianFoam, the swak4Foam library is required. This provides the groovyBC utility, which offers considerable flexibility for complex simulations [36,37]. Time control and solution I/O parameters are specified in system/controlDict, which also manages access to the groovyBC library. The system/fvSchemes dictionary configures numerical finite-volume discretization schemes, with temporal terms defaulting to the Euler method. The linear equation solver (default: GAMG) and other algorithmic controls are specified in the system/fvSolution dictionary.

2.1.3. Thermal modeling using electrical analogy

The thermal-electrical analogy provides deeper information that analytical models and experimental tests cannot obtain, particularly for determining heat fluxes and stored energy [26,38,39]. Unlike complex CFD modeling, this approach enables efficient unsteady heat transfer simulations without requiring fine computational

meshes or time-consuming procedures [38,39]. Table 2 summarizes the key analogies between thermal and electrical concepts.

Table 2. The two pairs of analogy between thermal and electrical equations [26,39]

Thermal	Electrical
1) Fourier's law: $\dot{Q}(t) = \frac{kA}{l}\Delta T(t)$	Ohm's law: $I(t) = \frac{1}{R}V(t)$
2) Heat equation applied to a body: $mc_p\frac{dT(t)}{dt} = \dot{Q}(t)$	Charge of a capacitor: $C\frac{dV(t)}{dt} = I(t)$

The first pair of equations establishes a direct thermal-electrical analogy between one-dimensional Fourier's law (governing thermal conduction) and Ohm's law (governing electrical conduction) [26,39]. Fourier's law expresses the conductive heat flux as $\dot{Q}(t)$ proportional to the temperature gradient $\Delta T(t)$, and inversely proportional to the thermal resistance, with the proportionality constant defined by the material's thermal conductivity, , cross-sectional area, A , and characteristic length, l . Analogously, Ohm's law relates electric current I(t) to voltage V(t) through electrical resistance R.

The second pair of equations formalize the analogy between thermal energy storage and electrical charge storage. Thermal energy storage is quantified as the heat capacity $C_{th} = m_{cp}$ (the product of mass, m, and specific heat capacity, c_p) multiplied by the temporal derivative of temperature $\frac{dT(t)}{dt}$. This corresponds to the heat flux ($\dot{Q}(t)$) required to induce temperature changes. Similarly, the charge storage in a capacitor is governed by $C\frac{dV(t)}{dt} = I(t)$ where C is the capacitance and I(t) is the current driving voltage changes.

While the lumped-capacitance approach simplifies transient thermal analysis, its validity depends critically on the Biot number ($Bi \ll 1$), which ensures negligible internal temperature gradients by assuming uniform temperature distribution within the object [26,27].

Following the methodology of Ramirez-Laboreo et al. [39], the cookstove is modeled as three components: the heating element (charcoal bed), the insulating element (clay), and the external cladding (stainless steel foil). In our readapted model diagram (Figure (1)), the heating element generates power to maintain a prescribed surface temperature $T_s(t)$ on the internal cavity. The insulating element (clay) is characterized by thermal resistance R_1, the cladding (stainless steel foil) by thermal resistance R_2, and the ambience by resistance to convection R_3.

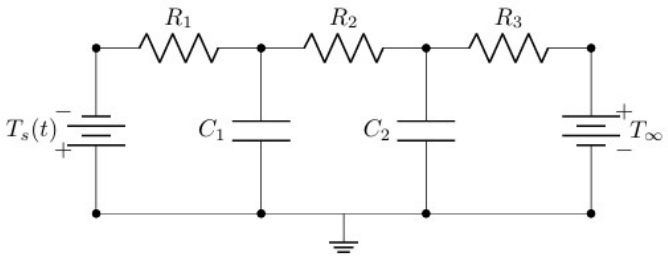

Figure 1. The heating element generates power, maintaining a time-dependent surface temperature $T_s(t)$ on the internal cavity that increases through resistance R_1 the temperature of the insulating element T_1 (modeled as capacitor C_1). The insulation partially transfers through resistance R_2 some energy to the cladding of the cooking stove (modeled as C_2). Finally, a fraction of the power dissipates to ambient temperature T_∞ through external resistance R_3

For a cylindrical cookstove, the thermal resistances are defined as:

$$R_1 = \frac{\ln(r_{o1}/r_i)}{2\pi kl}$$
$$R_2 = \frac{\ln(r_o/r_{o1})}{2\pi kl}$$
$$R_3 = \frac{1}{h \cdot 2\pi r_o l} \quad (8)$$

where r_i, r_{o1}, and r_o represent the combustion chamber radius, insulator outer radius, and cladding outer radius, respectively; l is the chamber height, and h is the convective heat transfer coefficient.

The thermal capacitances for the insulator (C_1) and cladding (C_2) are:

$$C_1 = \rho_1\pi(r_{o1}^2 - r_i^2)lc_{p1} \qquad C_2 = \rho_2\pi(r_o^2 - r_{o1}^2)lc_{p2} \quad (9)$$

where ρ_1, ρ_2 are material densities, and c_{p1} , c_{p2} are specific heat capacities.

The system is modeled in state-space form using Kirchhoff's rules, with the temperatures of the insulator and the cladding $T_1(t)$, $T_2(t)$ as state variables. The input is the imposed surface temperature $T_s(t)$, and the disturbance is ambient temperature T_∞ [39]:

$$\begin{bmatrix}\dot{T}_1(t)\\ \dot{T}_2(t)\end{bmatrix} = \begin{bmatrix}-\left(\frac{1}{C_1R_1}+\frac{1}{C_1R_2}\right) & \frac{1}{C_1R_2}\\ \frac{1}{C_2R_2} & -\left(\frac{1}{C_2R_2}+\frac{1}{C_2R_3}\right)\end{bmatrix}\begin{bmatrix}T_1(t)\\ T_2(t)\end{bmatrix} + \begin{bmatrix}\frac{1}{C_1R_1} & 0\\ 0 & \frac{1}{C_2R_3}\end{bmatrix}\begin{bmatrix}T_s(t)\\ T_\infty(t)\end{bmatrix} \quad (10)$$

$$\begin{bmatrix}y_1(t)\\ y_2(t)\end{bmatrix} = \begin{bmatrix}1 & 0\\ 0 & 1\end{bmatrix}\begin{bmatrix}T_1(t)\\ T_2(t)\end{bmatrix} \quad (11)$$

Here, the state vector, $x = [eT_1(t); T_2(t)]$ the output vector, $y = [y_1(t); y_2(t)]$, and $U = [T_s(t); T_\infty(t)]$ the input vector defines a

linear time-invariant (LTI) system. In Equation 11, the feedthrough matrix is the zero matrix as inputs $x = [T_s(t); T_\infty(t)]$ directly affect states but have no feedthrough to outputs. This state-space formulation enables numerical simulation via MATLAB/Simulink, leveraging its graphical interface for dynamic system analysis.

To analyze the stability of the state-space system, we first derive the characteristic equation from the state matrix and then construct the Routh table for this second-order system. From Equation (10), the eigenvalues (λ) of the system matrix satisfy:

$$\lambda^2 + \left(\frac{1}{C_1R_1} + \frac{1}{C_1R_2} + \frac{1}{C_2R_2} + \frac{1}{C_2R_3}\right)\lambda + \frac{1}{C_1C_2}\left(\frac{1}{R_1R_2} + \frac{1}{R_1R_3} + \frac{1}{R_2R_3}\right) = 0 \quad (12)$$

The Routh-Hurwitz criterion verifies that:

- All coefficients of the polynomial are present and share the same sign since $C_1, C_2, R_1, R_2, R_3 > 0$
- The first column of the Routh table exhibits no sign changes.

However, for our second-order system, this simplifies to a direct search for the roots (poles) of the characteristic equation. The Δ discriminant, after expansion and simplification, gives:

$$\Delta = \left(\frac{1}{C_1R_1} + \frac{1}{C_1R_2} - \frac{1}{C_2R_2} - \frac{1}{C_2R_3}\right)^2 + \frac{4}{C_1C_2R_2^2} \quad (13)$$

In our case, since $\Delta > 0$ (because of the presence of a squared term), this implies two distinct real roots, both strictly negative (since all coefficients in Equation (12) are positive). Thus, the system is asymptotically stable.

2.2. Radiation modeling between surfaces

2.2.1. Design specifications of cookstoves samples

Figure 2 shows four examples of batch-loaded charcoal stoves used to evaluate the radiative heat transfer from the combustion chamber lining to the pot bottom. These Jiko-type ceramic stoves were developed by a microenterprise initiative, supported by the Center for International Forestry Research (CIFOR) and the World Agroforestry Centre (ICRAF), to produce improved cookstoves in Kisangani, the Democratic Republic of Congo. The stoves are made from sheet metal framework with clay thermal insulation [21] for the combustion chamber and a perforated base, so air flow can be controlled beneath the grate by a door [5]. Metal fixtures mounted on the stoves bear the weight of the cooking pot and allow air to circulate through a small gap between the pot and the top of the combustion chamber. Combustion chambers (CC) occur in two forms: right-circular cylinders and inverted truncated cones (ITC). The traditional reference cookstove shown in Figure 2 was constructed from repurposed sheet metal. Its combustion chamber, 29 cm in diameter and 8 cm in height, is entirely covered with ventilation holes approximately 1 cm in diameter, regularly spaced at 0.5 cm intervals. The geometric details for all stoves are provided in Table 3.

Figure 2. Models of charcoal cookstoves

Table 3. Geometrical specifications of ceramic cookstoves models

Description	AFBC -KIS	BOYOMA	JIKO -BUTEMBO	ORBAGEN
Combustion Chamber shape	Cylinder	IT Cone	IT Cone	Cylinder
CC up inner radius (m)	0.100	0.100	0.100	0.100
CC low inner radius (m)	0.100	0.080	0.080	0.100
CC depth (m)	0.070	0.080	0.070	0.100
CC volume (m^3)	0.00220	0.00204	0.00178	0.00314
Insulation thickness (m)	0.040	0.050	0.040	0.040
Number of grate holes	19	18	20	17
Diameter of holes (m)	0.018	0.018	0.018	0.018
Cladding thickness (m)	0.001	0.001	0.001	0.001
Pot supports height (m)	0.010	0.010	0.010	0.010
Door dimensions (m)	0.160 x 0.060	0.150 x 0.050	0.130 x 0.070	0.130 x 0.060
Stove height (m)	0.230	0.230	0.230	0.230
Stove weight (kg)	6.5	7.2	5.6	4.5

2.2.2. Analysis of radiation exchange between passive surfaces

Radiation constitutes the dominant mechanism of heat transfer to cooking pots in charcoal-fueled cookstoves [40]. Geometric parameters – including combustion chamber geometry (shape, depth, and diameter) and pot support height – are accounted for by a dimensionless geometric parameter called the "view factor". This factor represents the fraction of the total incident radiation intercepted by the target surface [26,27,41–43]. The radiative heat transfer from the char bed using radiative network method is proposed in Zube [43]:

$$q_{char} = \frac{\sigma A_p \left(T_{char}^4 - T_p^4 \right)}{\frac{1 - \epsilon_{char}}{\epsilon_{char}} + \frac{2}{1 + F_{char-pot}}} \tag{14}$$

where σ is the Stefan-Boltzmann constant, ϵ_{char} the emissivity of char, $F_{char-pot}$ the view factor, A_p the pot bottom surface area, T_p the temperature of the pot, and T_{char} the temperature of the charcoal bed.

However, the intensity of radiative heat transfer from the char bed diminishes as the fuel in the combustion chamber is depleted. As this occurs, the thermal energy absorbed by the pot becomes increasingly governed by radiation emitted from the ember bed and by contributions from the interior surfaces of the combustion chamber. As depicted in Figure 3, the combustion chamber-pot configuration can be approximated as an inverted truncated cone (or a right-circular cylinder) that radiates onto a coaxially aligned disk located at a distance L. The system comprises three surfaces of interest, each characterized by distinct thermal and radiative properties: the combustion chamber side surface s of area A_s at temperature T_s with emissivity ϵ_s, the grate surface g of area A_g at temperature T_g with emissivity ϵ_g, and the pot base surface p of area A_p at temperature T_p with emissivity ϵ_p. The effective emissivity of the grate requires correction to account for radiative losses through its apertures, because a fraction of the incident irradiation is transmitted and dissipated.

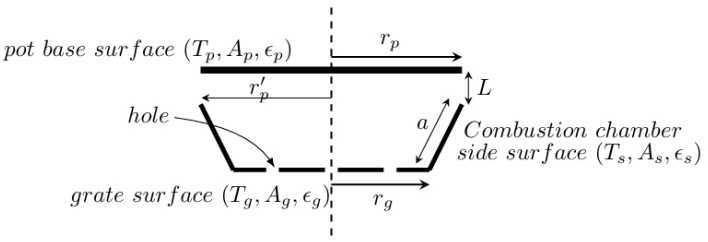

Figure 3. Combustion chamber - pot base surface configuration

Prior to evaluate radiative exchange between passive surfaces, several simplifying assumptions must be adopted [26,27]: (1) steady-state conditions prevail, implying time-invariant thermal behavior; (2) convective heat transfer is negligible compared to radiative transfer; (3) surfaces are gray and diffuse emitters and reflectors; (4) each surface in the cavity is isothermal, with spatially uniform radiosity and irradiation; (5) the medium within the enclosure is taken to be nonparticipating (a condition that becomes increasingly valid as fuel depletion progresses in the combustion chamber).

The radiative heat transfer analysis is initiated by calculating the geometric view factors between relevant surfaces. First, the view factor $F_{p-entrance}$, representing the radiative exchange between the pot's base and the combustion chamber entrance, is computed. Subsequently, the view factor, F_{p-g} quantifying radiative interactions between the pot's base and the combustion-chamber grate, is determined. To facilitate analytical evaluation of these view factors, the combustion chamber entrance is approximated as a hypothetical circular surface with radius r_p'.

The equation of the view factor F_{ij} for two coaxial parallel disks i and j, with respectively radius of r_i and r_j is given [26,27,42]:

$$R_i = r_i/L, \quad R_j = r_j/L, \quad S = 1 + \frac{1 + R_j^2}{R_i^2}$$
$$F_{ij} = \frac{1}{2}\left\{ S - \left[S^2 - 4\left(r_j/r_i \right)^2 \right]^{\frac{1}{2}} \right\} \tag{15}$$

After finding $F_{p-entrance}$ and F_{p-g}, we can use the summation rule to determine F_{p-s}, the view factor from the pot to the side wall. From the summation rule: $F_{p-s} = F_{p-entrance} - F_{p-g}$ and from reciprocity rule, we can additionally determine view factors, from the side wall to the pot F_{s-p}, , from the side wall to the grate, F_{s-g}, and from the grate to the pot, F_{g-p} .

Using the direct approach in [26,27,42], we can write for each of the three surfaces s, p and g :

$$\frac{\sigma T_{bi}^4 - J_i}{(1 - \epsilon_i)/(\epsilon_i A_i)} = \sum_{j=s,p,g} \frac{J_i - J_j}{1/(A_i F_{ij})} \tag{16}$$

where the J_i are the radiosities (emission + reflected irradiation) of each surface.

Equation (16) defines the radiative energy balance for the system. The left-hand side describes the radiative flux emitted by the surface, characterized by its surface resistance $(1 - \epsilon_i)\epsilon_i A_i$ term. This term is set equal to the right-hand side, which accounts for the net radiative exchange between the surface and all other surfaces via their corresponding geometrical resistances. The resulting formulation yields a system of three coupled linear algebraic equations that can be solved simultaneously for the unknown radiosities, J_p, J_s, and J_g. Once the radiosities are obtained, the net radiative heat transfer rate q_i for each surface can be computed using:

$$q_i = \frac{\sigma T_i^4 - J_i}{(1 - \epsilon_i)/(\epsilon_i A_i)} \tag{17}$$

2.2.3. Cookstoves performances and testing methods

To evaluate the impact of stove-pot configuration on radiation transfer to cooking pot, we conducted ISO 19867-1:2018(F) Water Heating Tests [24] and Controlled Cooking Tests [24,25]. The net calorific value of the charcoal (30250 kJ/kg) was determined using a Culture Instruments India LLP calorimeter in accordance with ISO 18125:2017. The average moisture content of the charcoal was 7%, with pieces averaging 3 cm x 3 cm x 3 cm in dimensions. For testing, we used a 22.5 cm-diameter × 19 cm-tall flat-bottom pot made of 0.8 mm-thick commercial aluminum and filled with 5 liters of water (without lid). All tests were performed using the ARC Laboratory Emissions Monitoring System (LEMS) in accordance with the ISO 19867-1:2018 Water Heating Test protocol. We conducted at least five replicate tests at two power levels: the high-power 'cold-start' phase (stove door fully open) and the low-power 'hot-start' phase (stove door fully closed). Each fuel-burning period lasted approximately 35 min. The primary ISO metrics evaluated were thermal efficiency, defined as the ratio of useful energy delivered to the total heat generated[24].

The Controlled Cooking Test (CCT), adapted from the Rob Bailis protocol [25], enabled fuel consumption comparisons between cookstove prototypes and the traditional reference stove. Evaluation involved two standard cooking tasks representative of typical Congolese daily meals: Test meal 1 — fufu, amaranth, and fried fish; Test meal 2 — rice, pondu (cassava leaves), and fried chicken. Meal quantities satisfied the nutritional requirements of an average seven-person household [44], with detailed meal compositions provided in Appendix B.

3. Results and discussions

3.1. Heat conduction modeling results

3.1.1. OpenFOAM-based simulations validation

In their experimental study, Kyuvi et al. [20] investigated the transient thermal response of a 0.028 m thick clay sample subjected to a constant heat flux of 773 K at its inner surface. The temperature evolution of the outer surface exposed to ambient conditions was recorded systematically. For numerical simulation, a simplified slab geometry was implemented in OpenFOAM's system/blockMeshDict, comprising a hexahedral block with dimensions 0.028 m × 0.001 m × 1 m in the x, y, and z directions. The mesh resolution was set to 28, 1, and 100 cells along the x-, y-, and z-axes, respectively. The thermophysical properties of clay are given in Table 4.

The front and back, and the top and bottom b.c.'s have been set to the fixed Gradient type with a zero gradient, since we do not consider heat conduction in these directions. The inner Wall b.c. has been set to the type fixed Value (uniform 773). The groovy BC utility was used to specify convective b.c. in the 0/T file. Under the operating conditions, a mean total convective heat transfer coefficient was estimated to h = 40 $W \cdot m^{-2} \cdot K^{-1}$ [45].

Table 4. Thermophysical properties of clay [26]

Property	Value
Density ($kg \cdot m^{-3}$))	1800
Specific thermal capacity ($J \cdot kg^{-1} \cdot K^{-1}$)	710
Thermal conductivity ($W \cdot m^{-1} \cdot K^{-1}$)	0.8
Emissivity	0.75

Figure 4 presents a comparative analysis of the temporal evolution of outer surface temperatures obtained experimentally and from OpenFOAM numerical predictions. The results demonstrate good agreement between experimental and simulated data, particularly in capturing the thermal transient behavior. The system achieves steady-state conditions at approximately 65 minutes, as evidenced by the temperature stabilization in both datasets. However, notable discrepancies are observed between 20 and 50 minutes into the heating process. These variations may be attributed to potential limitations in measurement techniques or instrumentation accuracy constraints, as discussed in [20].

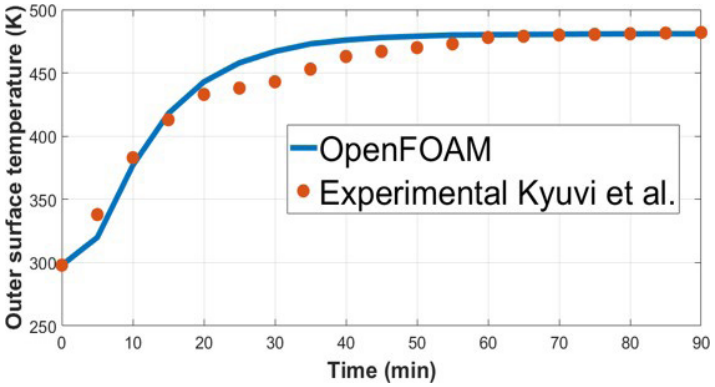

Figure 4. Outer surface temperature on a 0.028 m thick clay sample – Experimental [20] vs Open FOAM-predicted simulations

3.1.2. Transient cooling analysis: effect on the responsiveness of thermal mass

To examine the thermal responsiveness of the clay sample when placed near a heat source (or fire), we consider the following scenario. After the slab reaches steady-state conditions (as discussed in Section 2.1.1), a linearly decreasing temperature is imposed on the inner surface for simplicity: T (0, t) = 773 − 0.3 t, while the back surface remains exposed to ambient temperature (298 K). The one-dimensional temperature distribution within the slab during the cooling process is governed by the equations provided in Table 1. The key parameters include the initial hot-surface temperature B = 773 K and the cooling rate . A = -0.3K $\cdot$ s^{-1} Based on these conditions, the Biot number and thermal diffusivity are determined to be 1.2 and $2 \cdot 10^{-7} m^2 \cdot s^{-1}$ respectively.

A C++ program was developed to numerically evaluate the trigonometric series solution from Table 1 by solving the 1D heat conduction problem. A custom class was implemented to instantiate objects for computing the roots of the transcendental Equation (6) using the Newton-Raphson method.

A comparison between analytical solutions and OpenFOAM-based numerical predictions is presented in Figure 5. The results demonstrate excellent agreement between the steady-state analytical solution and the OpenFOAM simulation. For a mesh resolution of 1 mm and a time step of 0.01 s, the relative error between the analytical and numerical solutions remains below 3.0% at both 500 s and 1000 s of cooling.

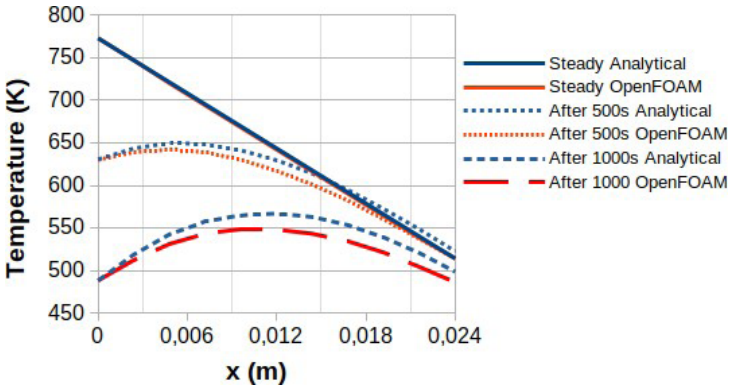

Figure 5. Temperature distribution in a clay lining slab as one end surface is subject to a decreasing temperature over time, and the opposite convective side is exposed to the ambient

The time lag t_1 is the delay between absorption and release of stored heat as the hot surface temperature decreases. It can be considered the time at which the decreasing temperature imposed on the boundary surface falls below that of the region adjacent to the boundary within the slab.

$$\left.\frac{\partial T(x,t)}{\partial x}\right|_{x=0} \geq 0 \tag{18}$$

To estimate t_1 for a linearly decreasing boundary temperature, we derive the trigonometric series solution T(x,t) (Equation (5)) with respect to x and set the derivative to zero. Retaining only the first term of the series (neglecting higher-order terms) and rearranging yields:

$$e^{-0.0007262 \cdot t} \approx 0.0004143 \cdot (t + 830.35) \tag{19}$$

Equation (19) is implicit with respect to time t, and its solution can be determined graphically. Yet, an exact closed-form solution can be obtained analytically using the Lambert W function (see [46]), which resolves transcendental equations of this form. The solution is expressed as follows:

$$t = -830.35 + \frac{1}{0.0007262} W\left(\frac{0.0007262 \cdot e^{-(0.0007262 \cdot x - 830.35)}}{0.0004143}\right) \tag{20}$$

where W is the product log function. From this, we compute an approximate reverse heat flow time of $t_1 = 429$ s.

When one boundary is perfectly insulated (zero heat flux) and the slab reaches steady state, heat is conducted toward regions of lower temperature.

3.1.3. Energy storage capacity: electrical analogy and OpenFOAM

This section investigates the energy storage capacity of a typical cookstove body using an electrical analogy and CFD simulations. The system under study consists of a cylindrical combustion chamber with a clay lining (inner radius $r_i = 0.114$ m; outer radius $r_{o1} = 0.138$m) and a stainless-steel cladding (thickness $\delta = 0.0008$ m). The thermophysical properties of the clay are provided in Table 4, while the stainless steel exhibits the following properties: a density (ρ_2) of 7500 kg m^{-3}, a specific heat capacity (c_{p2}) of 460 J $\cdot$ kg^{-1} $\cdot$ K−1, and a thermal conductivity (k_2) of 20 W $\cdot$ m^{-1} $\cdot$ K^{-1} [26].

Based on the electric block diagram in Figure 1, the thermal resistances R_1, R_2, R_3 were computed using Equation (8), while the thermal capacitances of the clay lining (C_1) and cladding (C_2) were derived from Equation (9). The system's state-space representation, given by Equations (10) and (11), simplifies Equations (21) and (22) under the selected assumptions.

$$\begin{bmatrix} T_1'(t) \\ T_2'(t) \end{bmatrix} = \begin{bmatrix} -0.8964 & 0.8953 \\ 9.0579 & -9.0725 \end{bmatrix} \begin{bmatrix} T_1(t) \\ T_2(t) \end{bmatrix} + \begin{bmatrix} 0.0011 & 0 \\ 0 & 0.0145 \end{bmatrix} \begin{bmatrix} 773 \\ 298 \end{bmatrix} \tag{21}$$

$$\begin{bmatrix} y_1(t) \\ y_2(t) \end{bmatrix} = \begin{bmatrix} 1 & 0 \\ 0 & 1 \end{bmatrix} \begin{bmatrix} T_1(t) \\ T_2(t) \end{bmatrix} \tag{22}$$

This electrical circuit was implemented in Simulink®, a MATLAB® graphical programming environment for model-based design. The system's asymptotic stability (evidenced by two poles with negative real parts) stems from interactions between its dual energy-storage elements:

- The clay insulator with its high thermal capacitance ($C_1 \approx 2.428 \times 10^4$ J $\cdot$ K^{-1}) and resistance ($R_1 \approx 0.0380$ K $\cdot$ W^{-1}), governing the slow pole ($\lambda_1 = -0.00231 s^{-1}$), very close to zero, meaning the system takes a long time to reach steady-state in the clay insulator after a disturbance. The time constant for the slow pole ($\tau_1 = 1/|\lambda_1| \approx 432$s ≈ 7 min) shows how high thermal mass resists rapid temperature changes, leading to slow dynamics.
- The steel cladding with negligible capacitance ($C_2 \approx 2.4 \times 10^3$ J $\cdot$ K^{-1})) and resistance ($R_2 \approx 4.599 \times 10^{-5}$ K $\cdot$ W^{-1}), tied to the fast pole ($\lambda_2 = -9.966 s^{-1}$). The time constant for the fast pole ($\tau_2 = 1/|\lambda_2|$) implies that this transient state dies out almost instantly (within ~0.1 s).

Concurrently, the thermal system was simulated using OpenFOAM's computational fluid dynamics (CFD) framework (see sections 2.1.2

and 3.1.1), employing the simpleFunctionObject utility to compute volume-averaged temperature fields. This methodological step involved integrating into the system/controlDict configuration file within the laplacianFoam case directory, the functions sub-dictionary of type volumeAverage. For 3D hollow cylindrical geometry generation, the blockMeshDict mesh descriptor file was configured using the #calc inline calculation directive, thereby enabling parametric mesh definition [33,37].

The clay temperature (T_1) and cladding temperature (T_2) were chosen as state variables for comparison between the electrical-analogy model and the OpenFOAM volume-averaged temperature profiles (Figure 6). The key observations emerging from this analysis show that the cladding's minimal product C_2R_2 ensures its temperature rapidly aligns with the insulator's T_1, leading to $T_1 \approx T_2$. Secondly, the lumped-capacitance approximation underestimates the temperature evolution predicted by OpenFOAM. This discrepancy arises because the electrical analogy assumes uniform temperature distribution, which is valid only for systems with a Biot number $Bi \ll 1$ [26,27].

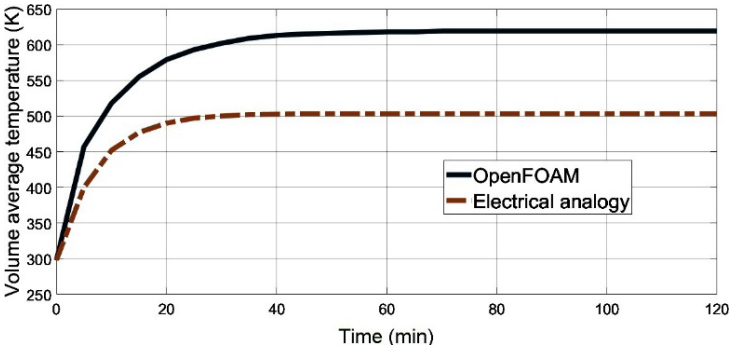

Figure 6. Volume average temperature of the clay lining: Electrical analogy and OpenFOAM

After ~ 35 minutes, energy losses become dominated by convective transfer to the ambient environment. To enhance the cookstove's heat storage capacity, the convective resistance can be increased by applying insulation materials to the clay lining [23]. Heavily insulating the back side eliminates conductive losses, thereby converts the inner surface into a re-radiating boundary (i.e., all incident radiation is re-emitted) [27,42].

3.2. Radiation transferred to pot from inner walls

3.2. 1. View factors, radiosities and net radiative heat transfer

Following the methodology outlined in Section 2.2.2 and using the geometric parameters from Table 3, we present the calculated view factors between the relevant surfaces in Table 5. All four analyzed cookstoves have identical top inner diameters (0.200 m) and pot support heights (0.010 m).

Table 5. View factors between surfaces across varied cookstoves geometries

View factor	AFBC-KIS (Cylinder)	BOYOMA (IT cone)	JIKO -BUTEMBO (IT cone)	ORBAGEN (Cylinder)
F_{s-p} (sidewall to pot)	0.32	0.42	0.46	0.28
F_{s-g} (sidewall to grate)	0.39	0.24	0.25	0.33
F_{g-p} (grate to pot)	0.46	0.30	0.33	0.35

A key distinction emerges between the truncated-cone and cylindrical combustion chambers:

- In truncated-cone designs, most radiative heat transfer to the pot bottom originates from the side walls because the angled surfaces direct heat upward.
- In cylindrical designs, the grate surface contributes significantly (flat base emits more upward radiation).

For the analysis of net heat exchange between surfaces, we assume an average steady-state temperature of 1000 K at the combustion chamber lining surface, consistent with experimental measurements reported by Zube [43], and a fixed pot-bottom temperature of 373 K (the boiling point of water) [47]. We consider surface emissivities of 0.75 for clay and 0.09 for the commercial aluminum pot [26,43].

We can first determine (Table 6) the radiosities, J_p, J_s and J_g, , from the set of the three algebraic Equations (16), and then evaluate (Table 7) the balances of the net radiation transfers, q_p, q_s and q_g, , exhibited by each of the three surfaces, using Equations (17).

Table 6. Radiosities of the three surfaces of interest

Radiosity ($W \cdot m^{-2}$)	AFBC-KIS	BOYOMA	JIKO -BUTEMBO	ORBAGEN
J_p (pot surface)	50363	50235	50253	50644
J_s (side surface)	56021	55850	55804	56161
J_g (grate surface)	55457	55110	55206	55898

Table 7. Net radiative heat transferred from surfaces

Power (W)	AFBC-KIS (Cylinder)	BOYOMA (IT cone)	JIKO -BUTEMBO (IT cone)	ORBAGEN (Cylinder)
q_p (pot surface)	-153	-153	-153	-154
q_s (side surface)	90	115	108	102
q_g (grate surface)	63	38	45	52

The contributions from the grate q_g and side walls q_s correlate well with the view factors in Table 5, validating the theoretical model. Moreover, we can discern the following pertinent observations:

- The net heat transfer rate at the bottom surface q_p is negative because the pot functions as an absorber. As a result, the net radiative balance of the three surfaces is zero.
- The net radiative heat transfer to the pot q_p remains remarkably invariant at 153 W (±0.5%) across all four cookstove designs, regardless of the combustion chamber's shape.

This insensitivity to chamber geometry variations can be explained by two fundamental principles of radiative heat transfer: energy balance in an enclosed system and view factor saturation. In an enclosed cavity, all thermal radiation emitted by a surface must be absorbed by other surfaces within the cavity. In cylindrical designs, a further increase in chamber depth enhances the sidewall's thermal contribution while reducing that of the grate, thus preserving the energy balance. Likewise, in inverted-cone combustion chambers, tilting the lateral wall increases the lateral wall's thermal contribution while reducing the grate's contribution due to the grate's decreased surface area. Additionally, the view factor between the cavity aperture and the pot approaches its maximum (~0.90) at short pot distances (0.010 m). At this point, the pot captures nearly the entire hemispheric radiation from the cavity [26,27,42].

While radiative net heat transfer (q_p) appears similar, the overall heat transfer efficiency to cooking pot fundamentally depends on the specific radiative efficiency (q'), a more meaningful metric that we define as:

$$q' = \frac{\text{Net radiative heat to pot}}{\text{Total cavity surface area}} \quad (20)$$

Table 8 ranks the cookstove designs according to this specific efficiency measure, providing clearer insight into their relative performance. Among the evaluated designs with fixed combustion-chamber top diameter and pot-support height, Jiko-Butembo exhibits the highest net radiative efficiency, followed by Boyoma; this performance is attributed to their reduced cavity surface areas.

Table 8. Net radiative heat delivered to pot per unit area of insulation surface

Power per unit area of cavity surface ($W \cdot m^{-2}$)	JIKO -BUTEMBO (IT cone)	BOYOMA (IT cone)	AFBC-KIS (Cylinder)	ORBAGEN (Cylinder)
q_p'	2722	2555	2195	1690

3.2.2. Thermal efficiency and fuel savings

Figure 7 presents the mean results of five Water Heating Test replicates, showing thermal efficiencies for the high-power (cold-start) and low-power (hot-start) phases and their combined average. These results align with the efficiency ranges reported by Boafo-Mensah et al. [5]. For comparative analysis:

- The traditional cookstove, lacking clay insulation, demonstrated a baseline thermal efficiency of 22% at a single power level.
- All four ceramic cookstoves exhibited superior performance, achieving 32–59% higher thermal efficiency than that of the traditional charcoal cookstove.

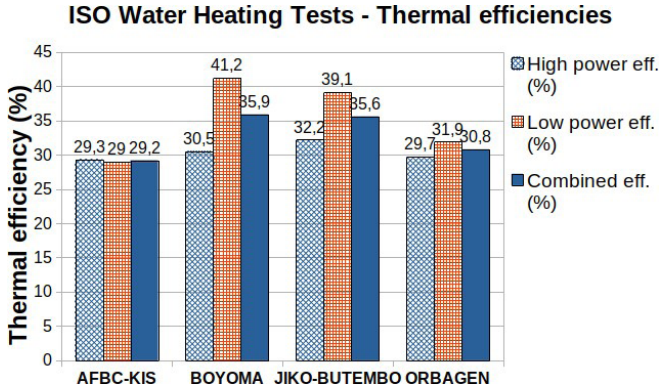

Figure 7. ISO thermal efficiency.

Specific radiative heat flux to the pot (Table 8) is closely related to the measured thermal efficiencies (Figure 7). Regarding stove-cooking-pot, inverted truncated-cone designs performed better. Their average thermal efficiencies are 20% higher than those of cylindrical counterparts. This performance advantage correlates with their reduced combustion chamber volumes (Table 3). Although small-volume combustion chambers emit the same net radiative heat from their surfaces as larger chambers achieve higher energy efficiency, delivering comparable thermal mass contributions while using significantly less fuel. JIKO-BUTOMBO (with the smallest chamber volume) exhibited a high peak efficiency of 32%. This finding supports Geskin's [48] second law of thermodynamics approach to optimizing fuel consumption for process heating applications.

Furthermore, truncated-cone designs exhibited 30% efficiency gains from the cold-start (high-power) to hot-start (low-power) phases (Figure 7). Extended heating periods benefit significantly from ther-

mal mass effects, enabling substantial fuel savings. This enhancement results from the following:

- Thermal mass effects during cold start (heat storage in stove body).
- Re-radiation dominance during hot start (heated surfaces acting as secondary emitters) [27,42].
- Minimized convective losses (ventilation door closed per ISO protocol [24]).

The 35-minute test duration (corresponding to steady-state attainment; see Section 3.1.3) indicated that combustion chamber volume and operating duration were more influential than shape-related effects in charcoal cookstoves. The combustion chamber volume and fuel burn duration emerge as key determinants of efficiency.

Controlled Cooking Tests were conducted to evaluate cookstove performance using standardized local cooking tasks. Figure 8 shows fuel consumption when cooking typical meals with different charcoal cookstoves, including the traditional cookstove. The peak in this energy demand is observed when using the traditional cookstove. The difference in energy demand between Test-Meal #1 and Test-Meal #2 is due to variations in cooking time and heating regimes.

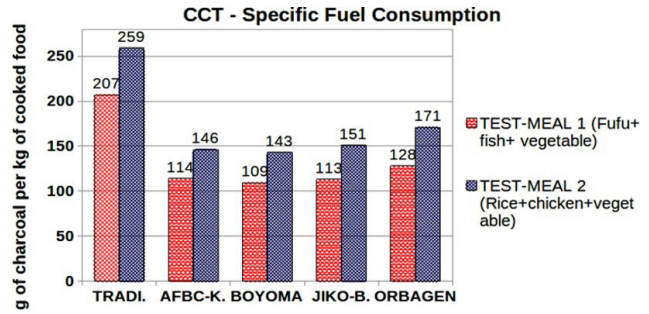

Figure 8. Specific fuel consumption of cookstoves

Figure 9 presents the fuel savings of improved cookstoves (34–47%) compared with traditional metal stoves. Results of the Controlled Cooking Tests corroborate those of the Water Heating Tests (ISO 19867-1). BOYOMA, AFBC-KIS, and JIKO BUTEMBO are more fuel-efficient in accordance with the previous observations [20-23].

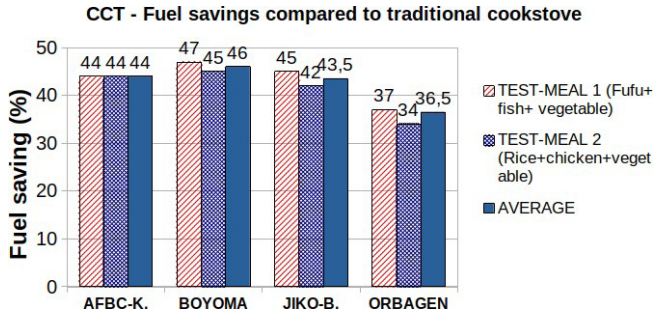

Figure 9. Fuel saving compared to the traditional cookstove

4. Limitations

Beyond the critical role of geometrical factors in cookstove performance, analyzing radiative heat transfer between the combustion chamber and pot surface presents multifaceted challenges. Key limitations include:

- Complex reaction kinetics and fluid flow dynamics within the reacting charcoal bed [40];
- Interplay of heat transfer modes: While radiation dominates, conductive and convective effects demand rigorous consideration [49,50];
- Participating media interactions: Charcoal particles, carbon dioxide, and water vapor in the combustion chamber absorb, reflect, or scatter radiation, contradicting the simplified assumption of a non-participating (transparent) medium [27,42].

The combustion chamber volume further complicates optimization, as it necessitates determining the minimum fuel quantity required for efficient operation. Geskin [48] addressed similar challenges in furnace design using second-law thermodynamics (exergy analysis), a methodology adaptable to cookstoves. These insights highlight critical research avenues, such as advanced multiphysics modeling of radiative-convective coupling and experimental validation of participating media effects in small-scale combustion systems [27,42].

5. Conclusion

This study systematically investigates the effects of thermal mass integration on heat transfer efficiency in charcoal cookstoves, with clay used as an insulating material. Our findings demonstrate that transient conduction and radiation exchange between passive surfaces significantly influence cookstove performance. While the net radiative heat absorbed by the cooking pot remains largely unaffected by combustion chamber shape, the chamber's volume and fuel burn duration emerge as key determinants of efficiency. Among the tested designs, stoves with inverted truncated-cone combustion chambers — which have smaller chamber volumes — delivered the best heating performance. Standard ISO Water Heating Tests and Controlled Cooking Tests confirmed that this optimized design achieves 20% higher thermal efficiency than in cylindrical chambers and achieves 34-47% fuel savings compared to the traditional metal stove. After sufficient heating, the clay thermal-mass effect becomes pronounced: the combustion chamber's inner surface increasingly functions as a re-radiating source, boosting efficiency. Specifically, truncated-conical stoves exhibit an average 30% increase in thermal efficiency when transitioning from the high-power 'cold-start' phase to the low-power 'hot-start' phase.

To support these insights, we also developed innovative modeling approaches combining transient conduction analysis (via a one-term approximation and the Lambert W function), heat-flux calculations using a lumped-capacitance method (electrical analogy), and radiation modeling between passive surfaces. These results provide

evidence-based design guidelines indicating that smaller combustion-chamber volumes improve efficiency and that material selection is crucial for thermal performance. By advancing cleaner, more efficient household energy solutions, this work directly supports Sustainable Development Goal (SDG)7. Future research should explore alternative insulating materials, optimize combustion chamber geometry, and develop strategies to improve material durability.

Appendices

Appendix A: 1-D transient heat conduction in a slab assuming no heat generation and time-dependent temperature variation at one boundary

Consider the transient heat diffusion equation:

$$\frac{\partial T}{\partial t} = \alpha \frac{\partial^2 T}{\partial x^2} \tag{A.1}$$

where α is the thermal diffusivity of the material ($m^2 \cdot s^{-1}$) defined as $\alpha = k/(\rho c)$, with denoting thermal conductivity ($W \cdot m^{-1} \cdot K^{-1}$), ρ the density ($kg \cdot m^{-3}$), and c the specific heat capacity ($J \cdot kg^{-1} \cdot K^{-1}$).

The system is governed by the following conditions:

Initial condition:

$$T(x,0) = f(x),\ 0 < x \leq L \tag{A.2}$$

Boundary conditions:

At x = 0:

$$T(0,t) = \varphi(t),\ 0 < t < \infty \tag{A.3}$$

At x = L (convective cooling):

$$-k\frac{\partial T}{\partial x}(L,t) = h\,[T(L,t) - T_\infty],\ t > 0 \tag{A.4}$$

Here, φ(t) represents a time-dependent temperature function is the convective heat transfer coefficient ($W \cdot m^{-2} \cdot K^{-1}$), and is the ambient temperature (K).

To simplify the boundary value problem, we introduce the substitution:

$$T^*(x,t) = T(x,t) - T_\infty \tag{A.5}$$

and decompose T* into steady-state (W*) and transient (v*) components:

$$T^*(x,t) = w^*(x) + v^*(x,t) \tag{A.6}$$

The steady-state solution $w^*(x)$ satisfies:

$$w^*(x) = T^*(0,t)\left(1 - \frac{h}{k + hL}x\right) \tag{A.7}$$

Substituting (A.6) into (A.1) yields the transient equation for v^*:

$$\frac{\partial v^*}{\partial t} = \alpha \frac{\partial^2 v^*}{\partial x^2} - T^*(0,t)_{,t}\left(1 - \frac{h}{k + hL}x\right) \tag{A.8}$$

with homogenized boundary conditions:

$$v^*(0,t) = 0 \tag{A.9}$$

$$hv^*(L,t) + k\frac{\partial v^*}{\partial x}(L,t) = 0 \tag{A.10}$$

$$v^*(x,0) = 0 \tag{A.11}$$

Note that the term $T^*(0,t)_{,t}$ represents the derivative of $T^*(0,t)$ in respect with time. Using eigenfunction expansion [28,31,32], the transient solution is expressed as:

$$v^*(x,t) = \sum_{n=1}^{\infty} \hat{v}_n^*(t)\sin(\mu_n x) \tag{A.12}$$

where $\mu_n L$ are roots of the transcendental equation:

$$\tan(\mu L) = -\frac{\mu L}{Bi} \tag{A.13}$$

With Bi the Biot number, by definition $Bi = \frac{hL}{k}$.

The source term $s(x,t) = -T^*(0,t)_{,t}\left(1 - \frac{h}{k + hL}x\right)$ can be expanded in terms of associated eigen functions such as:

$$s(x,t) = \sum_{n=1}^{\infty} \hat{s}_n \sin(\mu_n x) \tag{A.14}$$

Using orthogonality property to find $\hat{s}_n$:

$$\hat{s}_n = \frac{2T(0,t)_{,t}}{\mu_n L}\left[1 - \cos\mu_n L + \frac{Bi(\mu_n L\cos\mu_n L - \sin\mu_n L)}{(1 + Bi)\mu_n L}\right] \tag{A.15}$$

Applying derivatives to the series expansion, then substituting them in Equation (A.8), we have:

$$0 = \sum_{n=1}^{\infty}\left\{\frac{\partial \hat{v}_n^*(t)}{\partial t} + \alpha\mu_n^2\hat{v}_n^*(t) - \hat{s}_n\right\}\sin(\mu_n x) \tag{A.16}$$

Rearranging to get a single sum, and since the eigenfunctions are linearly independent, it follows that the coefficient of each basis function must always be zero t:

$$\frac{\partial \hat{v}_n^*(t)}{\partial t} + \alpha\mu_n^2\hat{v}_n^*(t) = \hat{s}_n \tag{A.17}$$

Multiplying both sides of the first order linear Equation (A.17) by an integrating factor $F = e^{\alpha\mu n^2 t}$, and integrating, the solution for $\hat{v}n^*$ becomes:

$$\hat{v}_n^*(t) = \frac{\hat{s}_n}{\alpha\mu_n^2}(e^{-\alpha\mu_n^2 t} - 1) \tag{A.18}$$

Taking the value of the series expansion coefficients of the source terms $\hat{s}_n$ of Equation (A.15) and insert it in (A.18):

$$\hat{v}_n^*(t) = \frac{2T^*(0,t)_{,t}}{\alpha\mu_n^3 L}\left[1 - \cos\mu_n L + \frac{Bi(\mu_n L\cos\mu_n L - \sin\mu_n L)}{(1+Bi)\mu_n L}\right](e^{-\alpha\mu_n^2 t} - 1) \quad (A.19)$$

And from Equation (A.12):

$$v^*(x,t) = \sum_{n=1}^{\infty}\frac{2T(0,t)_{,t}L^2}{\alpha(\mu_n L)^3}\left[1 - \cos\mu_n L + \frac{Bi(\mu_n L\cos\mu_n L - \sin\mu_n L)}{(1+Bi)\mu_n L}\right](e^{-\alpha\mu_n^2 t} - 1)\sin\mu_n x \quad (A.20)$$

where the summation extends over the positive roots of the transcendental Equation (A.13).

Reconsidering Equations (A.5), (A.6) and (A.18), the solution T(x,t) can be written:

$$T(x,t) = (T(0,t) - T_\infty)\cdot\left(1 - \frac{Bi}{(1+Bi)}\frac{x}{L}\right) + T_\infty + \sum_{n=1}^{\infty}\frac{2T(0,t)_{,t}L^2}{\alpha(\mu_n L)^3}\left[1 - \cos\mu_n L + \frac{Bi(\mu_n L\cos\mu_n L - \sin\mu_n L)}{(1+Bi)\mu_n L}\right](e^{-\alpha\mu_n^2 t} - 1)\sin\mu_n x \quad (A.21)$$

Appendix B: Controlled cooking tests meals ingredients

Table 9. Test-Meal #1: Fufu – Amaranth – Fried fish

Ingredient	Average weight of cooked meal per stove (g)
Fried fish (horse mackerel)	580
Amaranth	1900
Fufu	6800
Total weight	**9280**

Table 10**.** Test-Meal #2: Rice – Pondu (cassava leaves) – Fried chicken

Ingredient	Average weight of cooked meal per stove (g)
Fried chicken	585
Pondu (Cassava leaves)	2250
Rice	4800
Total weight	**7635**

List of abbreviations and nomenclature

A	Constant rate of cooling of the boundary surface of a slab ($K.s^{-1}$)
A_i	Area of surface i (m^2)
B	Initial temperature value on the boundary surface of a slab (K)
Bi	Biot number
C	Thermal capacitance ($W \cdot K^{-1}$)
c_p	Specific thermal capacity ($J \cdot kg^{-1} \cdot K^{-1}$)
F_{ij}	View factor
h	Heat transfer coefficient ($W \cdot m^{-2} \cdot K^{-1}$)
I	Current intensity (A)
J_i	Radiosity of surface i ($W \cdot K^{-2}$)
k	Thermal conductivity ($W \cdot m^{-1} \cdot K^{-1}$)
l	Height of the combustion (m)
L	Characteristic length (m)
$\dot{Q}$	Heat flux ($W \cdot m^{-2}$)
q_i	Power emitted by surface i ($W \cdot m^{-2}$)
q_i	Net radiative heat transferred from surfaces i
q'_p	Net radiative heat delivered to pot per unit area of insulation surface
r_i	Radius of element i (m)
R_i	Thermal resistance of element i ($W^{-1} \cdot K$)
s_i	Pole i (s^{-1})
t	Time (s)
t_l	Time corresponding to reverse heat flow (s)
T	Temperature (K)
T_i	Temperature of element i (K)
$\dot{T}_i$	Time derivative of temperature of element i (K)
T_∞	Ambient temperature (K)
V	Voltage (V)
W	Product log function
x	Cartesian coordinate

Greek symbols

Δ	The difference
Δ	The discriminant
α	Thermal diffusivity ($m^2 \cdot s^{-1}$)
ϵ_i	Emissivity of component
φ	Arbitrary time-dependent function of temperature
λ	eigenvalues of characteristic equation s^{-1}
ρ_i	Density of material
σ	Stefan-Boltzmann constant
τ	Time constant (s)
μ_n	Roots of the transcendental equation

Subscripts

p	pot base surface
s	Combustion chamber side surface
g	grate surface
i	Component of interest

Abbreviations

b.c.	Boundary condition
CC	Combustion chamber
ITC	Inverted-truncated cone combustion chamber

Authorship contributions

Conceptualization, L.M.A.; methodology, L.M.A., S.T.V and M.K.H.; software, L.M.A., S.T.V and M.K.H.; validation, L.M.A., S.T.V., M.K.H. and A.S.; formal analysis S.T.V., M.K.H. and A.S.; investigation, L.M.A, S.T.V., M.K.H., A.S. and N.N.B.; resources, N.N.B., M.K.H.; data curation, S.T.V. and M.K.H.; writing—original draft preparation, L.M.A.; writing—review and editing, L.M.A., S.T.V. and M.K.H.; visualization, S.T.V. and N.N.B.; supervision, S.T.V., M.K.H., A.S. and N.N.B. All authors have read and agreed to the published version of the manuscript.

Data availability statement

The authors confirm that the data supporting the findings of this study are available within the article. Raw data that support the findings of this study are available from the corresponding author upon reasonable request.

Conflict of interest

The author declared no potential conflicts of interest with respect to the research, authorship, and/or publication of this article.

Ethics

There are no ethical issues with the publication of this manuscript.

References

[1] A. K. Amegah and J. J. Jaakkola, "Household air pollution and the sustainable development goals," Bull World Health Organ, vol. 94, pp. 215–221, 2016, https://doi.org/10.2471/BLT.15.155812.

[2] IEA, "World Energy Outlook 2024," 2024.

[3] A. A. Putu Susastriawan, Y. Purwanto, B. W. Sidharta, and N. Siolimbona, "Thermal performance of cocoa pod cook stove," Journal of Thermal Engineering, vol. 10, pp. 188–195, 2024, https://doi.org/10.18186/thermal.1429918.

[4] A. R. Valentim, J. R. Behainne, and A. B. Junior, "Thermal Performance Analysis of Materials and Configurations for Cylindrical Sidewalls of Charcoal Kilns," Energies (Basel), vol. 15, p. 5872, 2022, https://doi.org/10.3390/en15165872.

[5] G. Boafo-Mensah, K. M. Darkwa, and G. Laryea, "Effect of combustion chamber material on the performance of an improved biomass cookstove," Case Studies in Thermal Engineering, vol. 21, p. 100688, 2020, https://doi.org/10.1016/j.csite.2020.100688.

[6] WHO, "WHO guidelines for indoor air quality: household fuel combustion," 2014.

[7] WHO, "Burning opportunity: clean household energy for health, sustainable development, and wellbeing of women and children," 2016.

[8] Berkeley Air Monitoring Group, "Monitoring and Evaluation of the Jiko Poa Cookstove in Kenya," 2013.

[9] J. M. Sagouong and G. Tchuen, "Mathematical Modelling of Traditional Stoves using the Thermal Network Approach," International Journal of Engineering Trends and Technology, vol. 58, pp. 1–9, 2018, https://doi.org/10.14445/22315381/IJETT-V58P201.

[10] FAO, "Regional wood energy development programme in Asia GCP/RAS/154/NET, Improved Solid Biomass Burning Cookstoves: A development manual," Bangkok, 1993.

[11] B. Haglund and K. Ratliff, "Thermal mass in passive solar and energy-conserving buildings," 2005.

[12] I. F. Odesola, E. O. Ige, and I. O. Yunus, "Design and Performance Evaluation of Energy Efficient Biomass Gasifier Cook Stove Using Multi Fuels," Journal of Energy Research and Reviews, pp. 1–7, 2019, https://doi.org/10.9734/jenrr/2019/v3i430103.

[13] K. Kaputo, M. Mwanza, and S. Talai, "A Review of Improved Cooker Stove Utilization Levels, Challenges and Benefits in Sub-Saharan Africa," Journal of Energy Research and Reviews, vol. 14, pp. 9–25, 2023.

[14] A. Yüksel, M. Arıcı, and H. Karabay, "Comparison of thermal response times of historical and modern building wall materials," Journal of Thermal Engineering, vol. 7, pp. 1506–1518, 2021, https://doi.org/10.18186/thermal.991093.

[15] M. Schumack, "A computational model for a rocket mass heater," Appl Therm Eng, vol. 93, pp. 763–778, 2016, https://doi.org/10.1016/j.applthermaleng.2015.10.035.

[16] N. A. MacCarthy, "A Zonal Model to Aid in the Design of Household Biomass Cookstoves," Iowa State University, 2013.

[17] M. Sedighi and H. Salarian, "A comprehensive review of technical aspects of biomass cookstoves," Renewable and Sustainable Energy Reviews, vol. 70, pp. 656–665, 2017, https://doi.org/10.1016/j.rser.2016.11.175.

[18] M. Bryden et al., "Design principles for wood burning cook stoves," Cottage Grove, OR ; London ; Washington DC, 2006.

[19] D. Still, A. Van Dam, and D. Ogle, "Homemade Insulation for stoves," n.d.

[20] E. Kyuvi, J. Nyangaya, and A. Aganda, "Improvement of Ceramic Insulation of Cook Stoves Using Carbonized Organic Waste," Journal of Energy Research and Reviews, vol. 14, pp. 51–64, 2023, https://doi.org/10.9734/jenrr/2023/v14i3286.

[21] M. Irro, C. Adihou, H. Ibrahim, A. Maza, C. Houngan, and M. Anjorin, "Effect of Thermal Mass on Fuel Consumption of Solid Biomass Cooking Stoves," Science Journal of Energy Engineering, vol. 12, pp. 48–58, 2024, https://doi.org/10.11648/j.sjee.20241203.13.

[22] J. Okino, A. J. Komakech, J. Wanyama, H. Ssegane, E. Olomo, and T. Omara, "Performance Characteristics of a Cooking Stove Improved with Sawdust as an Insulation Material," Journal of Renewable Energy, vol. 2021, pp. 1–12, 2021, https://doi.org/10.1155/2021/9969806.
[23] S. S. Ghiwe, V. R. Kalamkar, M. P. Kshirsagar, and P. D. Sawarkar, "The Influence of Stove Materials on the Combustion Performance of a Hybrid Draft Biomass Cookstove," Combustion Science and Technology, vol. 196, pp. 2380–2400, 2024, https://doi.org/10.1080/00102202.2022.2138710.
[24] ISO, "ISO 19867-1:2018/TR: Clean cookstoves and clean cooking solutions -- Harmonized laboratory test protocols -- Part 1: Standard test sequence for emissions and performance, safety and durability," 2018.
[25] R. Bailis, "Controlled Cooking Test (CCT), version 2.0," 2004.
[26] J. H. Lienhard, A heat transfer textbook. Phlogiston Press, 2003.
[27] F. P. Incropera, Fundamentals of heat and mass transfer. John Wiley, 2007.
[28] M. N. Özışık, Heat conduction. Wiley, 1993.
[29] H. S. Carslaw and J. C. Jaeger, Conduction of heat in solids. Clarendon Press, Oxford University Press, 2011.
[30] T.-W. Tu and S.-Y. Lee, "Analytical Solution of Heat Conduction for Hollow Cylinders with Time-Dependent Boundary Condition and Time-Dependent Heat Transfer Coefficient," J Appl Math, vol. 2015, pp. 1–9, 2015, https://doi.org/10.1155/2015/203404.
[31] D. L. Powers, Boundary value problems: and partial differential equations. Elsevier/Academic Press, 2010.
[32] W. E. Boyce and R. C. DiPrima, Elementary differential equations and boundary value problems. Wiley, 2001.
[33] C. J. Greenshields, "OpenFOAM User Guide version 7," 2019.
[34] F. Moukalled, L. Mangani, and M. Darwish, The finite volume method in computational fluid dynamics: an advanced introduction with OpenFOAM® and Matlab®. Springer, 2016.
[35] C. Degroot, "Understanding the OpenFOAM Case Structure," 2020.
[36] QdotSystems, "Heat transfer, OpenFOAM," 2023.
[37] OpenFOAM Wiki, "Contrib/groovyBC," n.d., http://openfoamwiki.net/index.php/Contrib_groovyBC (accessed July 27, 2023).
[38] D. Silva, "Modeling the Transient Response of Thermal Circuits," Applied Sciences, vol. 12, p. 12555, 2022, https://doi.org/10.3390/app122412555.
[39] E. Ramirez-Laboreo, C. Sagues, and S. Llorente, "Thermal modeling, analysis and control using an electrical analogy," in 22nd Mediterranean Conference on Control and Automation, IEEE, 2014, pp. 505–510, https://doi.org/10.1109/MED.2014.6961423.
[40] R. B. Mehrabian, "CFD Simulation of the Thermal Conversion of solid biomass in packed bed furnaces," Graz University of Technology, 2013.
[41] A. Chomcharn, "Improved Biomass cooking Stove for Household Use," Thailand, 2010.
[42] C. Balaji, Essentials of radiation heat transfer. Springer, 2021.
[43] D. J. Zube, "Heat Transfer Efficiency of Biomass Cookstoves," Colorado State University, 2010.
[44] Ministère du Plan, "RAPPORT GLOBAL, Enquête 1-2-3 : Résultats de l'enquête sur l'emploi, le secteur informel et sur la consommation des ménages/2012," 2014.
[45] Engineers Edge, "Convective Heat Transfer Convection Equation and Calculator," 2024.
[46] I. Kesisoglou, G. Singh, and M. Nikolaou, "The Lambert function should be in the engineering mathematical toolbox," Comput Chem Eng, vol. 148, p. 107259, 2021, https://doi.org/10.1016/j.compchemeng.2021.107259.
[47] L. M. Augustin, S. T. Vertomene, N. N. Bernard, A. Sadiki, and M. K. Haddy, "A New Perspective on Cooking Stove Loss Coefficient Assessment by Means of the Second Law Analysis," Entropy, vol. 24, p. 1019, 2022, https://doi.org/10.3390/e24081019.
[48] E. S. Geskin, "Second law analysis of fuel consumption in furnaces," Energy, vol. 5, pp. 949–954, 1980.
[49] Ö. Açikgöz, "Determination Of Convective, Radiative, And Total Heat Transfer Characteristics Over A Radiant Heated Ceiling: A Computational Approach," Journal of Thermal Engineering, vol. 5, pp. 372–384, 2019, https://doi.org/10.18186/thermal.623191.
[50] M. Tekkalmaz, Ç. Timuralp, and Z. Sert, "The Effect Of The Use Of Different Cover Materials On Heat Transfer In Flat Solar Collectors," Journal of Thermal Engineering, vol. 6, pp. 829–842, 2020, https://doi.org/10.18186/thermal.800158.